An evaluation by laser Doppler anemometry of the correction algorithm based on Kaimal co-spectra for high frequency losses of EC flux measurements of CH_4 and N_2O

P.S. Kroon[a,b]
A. Schuitmaker[a]
H.J.J. Jonker[a]
M.J. Tummers[a]
A. Hensen[b]
F.C. Bosveld[c]

[a]Delft University of Technology (TU Delft), Delft, The Netherlands
[b]Energy research Centre of the Netherlands (ECN), Petten, The Netherlands
[c]Royal Dutch Meteorological Institute (KNMI), De Bilt, The Netherlands

Published in Agricultural and Forest Meteorology 150 (2010) 794–805

ECN-W--10-029 March 2010

Agricultural and Forest Meteorology 150 (2010) 794–805

Contents lists available at ScienceDirect

Agricultural and Forest Meteorology

journal homepage: www.elsevier.com/locate/agrformet

An evaluation by laser Doppler anemometry of the correction algorithm based on Kaimal co-spectra for high frequency losses of EC flux measurements of CH_4 and N_2O

P.S. Kroon [a,b,*], A. Schuitmaker [a], H.J.J. Jonker [a], M.J. Tummers [a], A. Hensen [b], F.C. Bosveld [c]

[a] Delft University of Technology (TU Delft), Department of Multi-Scale Physics, Research Group Clouds, Climate and Air Quality, Lorentzweg 1, 2628 CJ Delft, The Netherlands
[b] Energy research Centre of the Netherlands (ECN), Department of Air Quality and Climate Change, Westerduinweg 3, 1755 LE Petten, The Netherlands
[c] Royal Dutch Meteorological Institute (KNMI), Section Atmospheric Research, Wilhelminalaan 10, 3732 GK De Bilt, The Netherlands

ARTICLE INFO

Article history:
Received 19 November 2008
Received in revised form 3 July 2009
Accepted 31 August 2009

Keywords:
CH_4 fluxes
High frequency losses
Kaimal spectrum
Laser Doppler anemometry
N_2O fluxes
Quantum cascade spectrometry

ABSTRACT

Eddy covariance (EC) technique is often used to determine greenhouse gas exchange at the earth's surface. In general, the instruments involved have a limited high frequency response which reduces the ability to detect the contribution to the flux of small eddies and in addition sensor separation gives high frequency losses. These missing contributions cause an EC flux underestimation which increases for higher values of the stability parameter *z/L*. Corrections can be performed based on the (empirical) Kaimal co-spectra; however, these were derived using instruments with a limited frequency response. In this study, the validity of the Kaimal spectrum during stable atmospheric conditions is assessed using laser Doppler anemometry (LDA) measurements of the vertical wind velocity at 1 m height during several stable nights at Cabauw in the Netherlands. LDA provides a means to determine the entire turbulent energy spectrum, i.e., from the production scale down to the dissipation scale. Since the measured spectra are found to be in good agreement with the Kaimal spectra, we assume that the Kaimal co-spectra are valid as well. Next, the effect of high frequency correction based on Kaimal co-spectra is assessed using 1 month of EC flux data of CH_4 and N_2O measured by quantum cascade laser (QCL) spectrometry at Reeuwijk in the Netherlands. After correction, the cumulative emissions increased about 15% for both gases. This underlines the importance of correcting for high frequency losses.

1. Introduction

During the last decade, climate change has become an important societal issue. Accurate measurements of trace gas fluxes and energy fluxes are very important for the study of environmental, biological and climatological controls of net surface exchange between ecosystem and atmosphere. EC flux measurements are often used to estimate the integrated emission on a hectare scale with a continuous coverage in time (e.g., Fowler et al., 1995; Laville et al., 1999; Veenendaal et al., 2007; Hendriks et al., 2008). For temperature and moisture, the EC technique can be evaluated independently using the energy balance closure. It has been shown that this balance is not always closed and fractional imbalances are larger at night than during daytime (e.g., Wilson et al., 2002; Kroon, 2004). This result indicates that scalar fluxes might be underestimated systematically. Therefore, all possible causes of the non-closure should be explored in more detail. Possible reasons are, among others, the assumption of no advection, high frequency losses due to damping in the tube, sensor separation and limited response time.

Many researchers apply a high frequency correction to turbulent fluxes to account for the effect of missing eddies. An Ogive based algorithm, described by, e.g., Aubinet et al. (2000) and Ammann et al. (2006) is often used for correcting these high frequency losses. This method is based on a comparison of the co-spectrum of temperature flux with the co-spectrum of CH_4 flux or N_2O flux. Kroon et al. (2007) showed that the high frequency losses are almost negligible up to the 2 Hz cut-off frequency of the quantum cascade laser (QCL) spectrometer using this Ogive algorithm. Therefore, no corrections were applied for the high frequency losses. However, these analyses were restricted to just a few cases in neutral atmospheric conditions and the losses were not evaluated for frequencies in the range between 2 Hz and the Kolmogorov scale.

Several other studies have reported on correction algorithms for high frequency losses using the empirical Kaimal co-spectra (Kaimal et al., 1972), e.g., Kristensen and Fitzjarrald (1984), Moore (1986), Bosveld (1999) and Aubinet et al. (2000). However, it is not

* Corresponding author at: Energy research Centre of the Netherlands (ECN), Department of Air Quality and Climate Change, Westerduinweg 3, 1755 LE Petten, the Netherlands. Tel.: +31 224 564062; fax: +31 56 8488.
E-mail address: p.kroon@ecn.nl (P.S. Kroon).

0168-1923/$ – see front matter © 2009 Elsevier B.V. All rights reserved.
doi:10.1016/j.agrformet.2009.08.009

certain whether the spectral shape of the Kaimal co-spectra is correct down to the dissipation scale since these spectra were derived using sonic anemometry with which not all small-scale contributions could be detected. The uncertainty in the spectral shape from production scale down to dissipation scale is larger for stable atmospheric conditions than for unstable conditions since the turbulent length-scale decreases (e.g., Van der Wiel et al., 2008) making the high frequency spectral contributions more prominent. In addition, during stable to very stable conditions buoyancy can affect isotropy (promoting 'pancake' eddies) and therefore possibly modify the spectral shape. Since the relative effect of non-detected eddies on the flux is supposed to be larger during stable conditions than during unstable conditions, it is important to validate the Kaimal co-spectra during stable conditions.

Because of that, the first goal of this study is to check the validity of the spectral shape of Kaimal spectra in the high frequency range during stable atmospheric conditions. The present evaluation is however limited to the vertical wind velocity (w) spectrum since our measurement technique is limited to one wind-component and techniques are not capable of sampling, e.g., CH_4 and N_2O down to the dissipation scale. However, the validity of the vertical wind velocity spectrum is the most critical check since the vertical velocity is most directly influenced by buoyancy effects; in other words, if thermal stratification is to have an influence on (co)-spectra, this must be most clearly visible in the vertical velocity spectrum. For a tracer gas (passive scalar) the effect will be less pronounced than in the w-spectrum. Therefore, if the Kaimal vertical velocity spectra are found to be in good agreement with the measured w-spectra, it will be reasonable to assume that the Kaimal co-spectra are valid as well.

Several measurement techniques are available for measuring the vertical wind velocity spectrum. The sonic anemometer is commonly used for EC flux measurements. This instrument is very reliable and robust. However, the smallest scale that can be detected is about the path length (usually 0.15 m). Hot-wire anemometry (HWA) is a technique that can detect smaller scales than sonic anemometry, even to the Taylor scale (Gulitski et al., 2007). However, it is not easy to carry out HWA measurements in the atmosphere since the wires are very fragile and there is a serious drift requiring multiple calibrations. In this study, the vertical wind velocity fluctuations are determined using both laser Doppler anemometry (LDA) and sonic anemometry. LDA works well under laboratory conditions (e.g., Snyder and Castro, 1998; Tummers et al., 2007). The technique is ideally suited for turbulence measurements, since LDA provides a non-intrusive means to determine the entire turbulent energy spectrum, i.e., from the production scale down to the dissipation scale. Drawbacks of LDA are the complexity of the system, the costs and the technical aspects of bringing seeding particles in the measurement area. We have developed an LDA system that is capable of operating under atmospheric conditions and have performed measurements with it at a grassland site at Cabauw in the Netherlands during several nights in 2008. We determine the variance spectrum of the vertical wind velocity at a height of 1 m using both LDA and sonic anemometry and compare these with the Kaimal spectra. Next, we focus on the correction algorithm based on Kaimal co-spectra and we assess its effect using 1 month of CH_4 and N_2O EC flux data measured at Reeuwijk in the Netherlands.

2. Experimental site and climatic conditions

The measurements have been conducted at a grassland site located near the village Cabauw, in the Netherlands (51°58′12.73″N, 4°55′34.98″E). To avoid flow obstruction, all instrumentation was placed at a distance of about 250 m from the main building. The measurement field consists of meadows and narrow ditches which are on average 40 m apart. The water level in the ditches is kept at about 0.40 m below the surface (Beljaars and Bosveld, 1997). The grass height ranges from 0.03 to 0.30 m. We have carried out the LDA measurements during five nights in the period from February to July 2008. Table 1 summarizes the periods and their atmospheric conditions. The stability is characterized by z/L with z the measurement height and L the Monin–Obukhov length scale. The stability was determined using both profile measurements and EC flux measurements, but the resulting stability parameters differ significantly in both methods, probably owing to the strong stability. The Monin–Obukhov length scale varied between $z/L = -0.01$ and 0.41 at 13 February 2008 and 17 June 2008, respectively, using the profile method. In addition, we use the difference between downward and upward long wave radiation LW for a characterization of the cooling of the nocturnal boundary-layer where values below $-50\ W\ m^{-2}$ indicate cloudless conditions. Radiation measurements were performed at a height of 1.5 m. It was cloudy during 8 February and 7 April 2008. The micrometeorological measurements were made available by the KNMI.

In addition, we have performed EC flux measurements of CH_4 and N_2O at an intensively managed dairy farm in 2007. This farm is located at Oukoop near the town of Reeuwijk in the Netherlands (52°02′11.22″N, 4°46′49.53″E). The terrain around the measurement tower was flat and free of obstruction for at least 600 m in all directions, except for the container in which the QCL was placed (20 m North-East from the tower). Manure and fertilizer are applied about five times a year from February to September. In addition, there are about four harvest events. Cow manure and artificial fertilizer application were about $55\ m^3\ ha^{-1}$ ($253\ kg\ N\ ha^{-1}\ yr^{-1}$) and $370\ kg\ ha^{-1}$ ($100\ kg\ N\ ha^{-1}\ yr^{-1}$) in 2006. In this study, we assess the effect of high frequency losses using 1 month data from 14 September 2007 to 12 October 2007. The average temperature and the average weekly precipitation were about 11.6 °C and 14 mm, respectively. Cow manure was applied on 15 September 2007 with an amount of $46\ kg\ N\ ha^{-1}$. More information about the measurement site can be found in Veenendaal et al. (2007).

Table 1
Description of the atmospheric conditions during the measurement nights at Cabauw in the Netherlands in 2008. Shown are wind speed U, air temperature T_{air}, net long wave radiation LW and stability parameter z/L where z denotes the measurement height and L the Monin–Obukhov length scale. The measurement heights are indicated in the subscripts.

	8 February	13 February	7 April	17 June	18 June
Start time (UTC)	08-02 19:10	13-02 20:40	07-04 21:30	17-06 22:40	19-6 00:30
End time (UTC)	08-02 22:40	13-02 23:30	07-04 22:40	18-06 01:30	19-6 02:40
U_{10m} ($m\ s^{-1}$)	3.6	2.5	2.7	2.3	2.6
$T_{air.10m}$ (°C)	6.8	1.5	3.6	13.4	15.1
$LW_{1.5m}$ ($W\ m^{-2}$)	−47	6	−45	−30	−15
z/L_{10m}[a] (−)	0.04	−0.01	0.23	0.41	0.07
z/L_{3m}[b] (−)	0.11	0.00	0.81	1.14	0.19

[a] Measured by the profile method using 2 and 10 m data.
[b] Measured by the EC flux method at 3 m height.

3. Instrumentation and methodology

3.1. Instrumentation

We aim to test the validity of the Kaimal spectrum of the vertical wind velocities under stable atmospheric conditions with LDA measurements. LDA is mainly used in laboratories and is hardly ever used for atmospheric measurements. However, this technique is ideally suited for turbulence measurements because of its non-intrusive nature and its high temporal and spatial resolution. In LDA, the Doppler-shift is measured of laser light scattered by small tracer particles that are carried along with the flow. The particle velocity v_p can be determined from the Doppler-shift, and this velocity is equal to the fluid velocity when the tracer particles are small enough. The basic principle of a dual-beam LDA is frequently described by the "fringe model". A single line from a continuous laser is split into two parallel laser beams (Fig. 1a). The two beams are focused to form the measurement volume at the beam crossing. This measurement volume is usually on the order of 0.1 mm in diameter and 1 mm in length. An interference pattern, the fringe pattern, is formed in the measurement volume with equally spaced fringes (Fig. 1b).

The light and dark bands are parallel to the bisector of the beams. The distance between two successively dark bands is given by the fringe distance d_f which can be computed by (Absil, 1995)

$$d_f = \frac{\lambda_0}{2\sin(\theta_L/2)} \tag{1}$$

where λ_0 denotes the wavelength of the incident laser light and θ_L the angle between the two laser beams. When a small particle crosses the fringe pattern, it scatters light and the intensity of the scattered light varies periodically with time. The frequency of this intensity variation is proportional to the velocity of the particle normal to the fringes, i.e., $v_p = f_D d_f$. To determine the Doppler frequency f_D, the scattered light is collected by a lens and then focused on the photomultiplier. The photomultiplier output signal has a periodic signal that oscillates with the Doppler frequency f_D. The photomultiplier output is fed to an LDA signal processor, which determines the Doppler frequency.

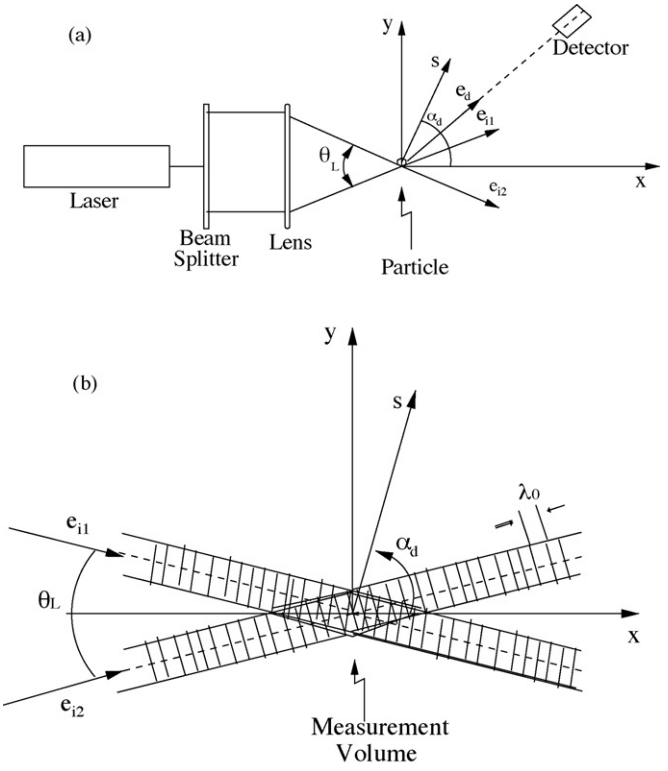

Fig. 1. (a) Schematic representation of dual-beam LDA system and (b) the interference pattern created by two laser beams. Where s denotes the velocity vector of the seeding particle, e_d the unit vector indicating the direction of the scattered light falling on the detector, e_{i1} and e_{i2} the unit vectors indicating the direction of the incident beams, λ_0 the wavelength of the laser light and θ_L the angle between both beams.

Particles that move with the same velocity magnitude in either forward or reverse direction through the measurement volume produce identical Doppler frequencies. To resolve this problem, we use a pre-shifting technique in which one of the incident beams is frequency pre-shifted by a constant frequency f_{sh}. This is accomplished by using an acousto-optic Bragg cell. As a consequence, the relationship between the particle velocity and the Doppler frequency reads

$$v_p = (f_D - f_{sh}) d_f, \tag{2}$$

and negative velocities can be distinguished from positive velocities, provided that the value of f_{sh} is larger than the Doppler frequency corresponding to the lowest anticipated velocity.

A potential source of error in LDA arises from the so-called velocity bias. This bias occurs due to a correlation between the instantaneous velocity and the number of particles passing the measurement volume per unit time. As a result, statistical quantities such as the mean velocity and the velocity variance are biased when computed as arithmetic averages. Weighting factors are used to compensate for the effects of the velocity bias. The mean velocity and variance are then computed from

$$\tilde{v} = \frac{\sum_{i=1}^{N} v_i \mathrm{tr}_i}{\sum_{i=1}^{N} \mathrm{tr}_i}, \overline{v'^2} = \frac{\sum_{i=1}^{N} v_i' 2\mathrm{tr}_i}{\sum_{i=1}^{N} \mathrm{tr}_i} \tag{3}$$

where tr_i is the transit time, i.e., the time a particle needs to transverse the measurement volume. The maximum frequency that can be detected accurately in the power spectrum with LDA is dependent on the number of samples and the mean sampling frequency.

The application of LDA in the atmosphere requires a different approach than application in the laboratory. For field measurements mobility is very important and a compact system is required. LDA systems used in laboratory commonly operate on powerful (1–10 W) Argon-ion lasers which have a very high power current (typically 360 V, 30 A). These systems are very large, need a high voltage network and large amount of cooling water. Therefore, we developed a more compact system (Fig. 2a) that uses a diode pumped solid-state laser with a wavelength of 532 nm, which did not need a high power voltage and water-cooling. The laser beam was split by a beam-splitter to obtain two laser lines. Two acousto-optic Bragg cells (model AOM-40, IntraAction Corp., USA) were driven at slightly different frequencies (40.0 and 40.5 MHz) to produce an effective frequency pre-shift of 0.5 MHz. The scattered light was collected in a 10° off-axis forward direction with a 350 mm focal length lens and then focused on a photomultiplier (Dantec). The photomultiplier output signal was fed to a TSI IFA 750 processor that determined arrival time, Doppler frequency, and transit time of each particle that moved through the measurement volume.

In addition, we changed the seeding strategy to make it suitable for atmospheric LDA measurements. External particles were entrained in the flow since the ambient aerosols were not numerous enough to perform measurements. To this end we generated tracer particles with a smoke machine that employed a fluid based on water and glycol. The particle diameter was approximately 1 μm. The seeding particles were injected into the atmospheric flow at a distance of about 25 m upstream of the measurement location using either a 20 m long circle segment (on 8 February and 13 February 2008) or a 60 m long circular segment (on 7 April, 17 June and 18 June

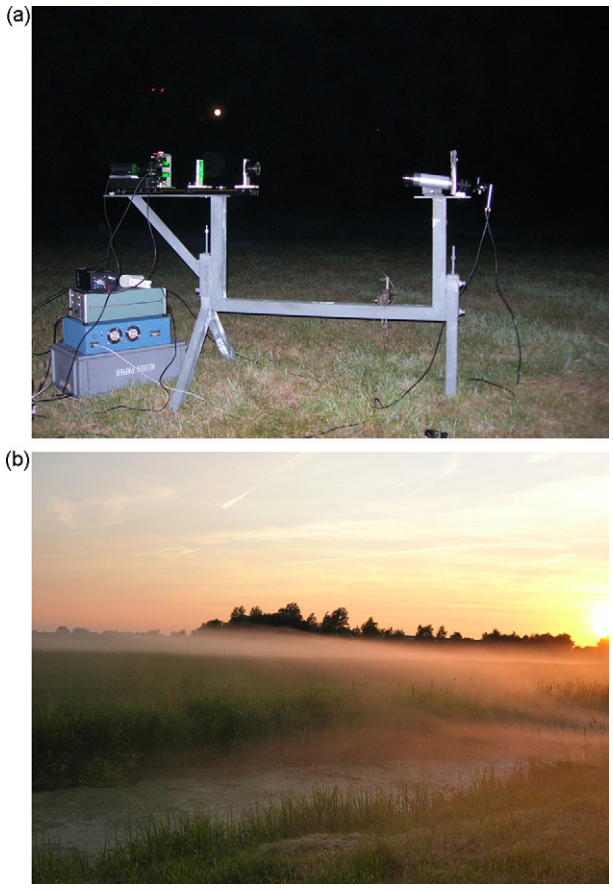

Fig. 2. (a) Picture of the LDA measurement set-up and (b) the fog caused by the seeding particles.

2008). Fig. 2b shows a photo of the fog caused by the seeding particles. More information about the measurement system and seeding strategy can be found in Schuitmaker (2008).

We examined the quality of the LDA measurements using a sonic anemometer (model TR90AH, Kaijo Denki, Japan) with a path length of 0.05 m. The sample rate was set to 40 Hz. Both probes were placed at a height of 1 m and they were both aligned with the mean horizontal wind direction. The lateral distance between both instruments was about 1 m, large enough to avoid interference and small enough to have the same footprint. The sonic anemometer measures transit times of high frequency pulses over three paths from which the three-dimensional wind velocity is computed (Schotanus et al., 1983). A potential source of error in measurements by a sonic anemometer arises from flow distortion due to transducers and the frame that supports them. When the wind direction is close to the direction of the measurement path, the transducers generate a wake, which can lead to a serious underestimation of the wind velocity components. The problem of flow distortion has received a lot of attention in the literature, e.g., Schotanus et al. (1983) and Wyngaard and Zhang (1985). Therefore, the sonic anemometer was calibrated for wind speed and angle on-flow. Corrections were applied following Kraan and Oost (1988). The sonic anemometer was also corrected for tilt error using the 2D rotation method (Wilczak et al., 2001). The first rotation in the horizontal plane ensures that the coordinate system is oriented along the mean wind direction and in the second rotation the coordinate system is tilted such that $\bar{w} = 0$. Both rotations ensure that the stream wise velocity component is aligned with the direction of the mean 3D vector.

The highest frequency that can be resolved by the Fourier transform is the Nyquist frequency, which is equal to half the sampling frequency. If filtering is applied to the sonic signals, the cut-off frequency f_c of the filter is usually chosen slightly less than the Nyquist frequency. However, high frequency losses occur due to line averaging along the path. The attenuation is 10% with eddy sizes approximately equal to πd (Kristensen and Fitzjarrald, 1984; Van Dijk, 2001) where d denotes the path length, resulting in a maximum frequency of $f_{\max}^{\text{Sonic}} = U/\pi d$. In this study, we set the cut-off frequency f_c to $f_{\max}^{\text{Sonic}}$.

We measured the EC fluxes of CH_4 and N_2O with a system consisting of a three-dimensional sonic anemometer (model R3, Gill Instruments, Lymington, UK) and a QCL spectrometer (model QCL-TILDAS-76, Aerodyne Research Inc., Billerica MA, USA) at Reeuwijk in the Netherlands. This sonic anemometer has a path length of 0.15 m and the sampling frequency was set to 20.8 Hz. It has three intersecting measurement paths with a non-orthogonal arrangement with 120° intervals around the vertical axis of the instrument. Each path has an angle of 45° with the horizontal axis. The measurement height was 3 m and the mast was positioned in the middle of the field. We used a 25 m polyethylene inlet tube with a diameter of 6.35×10^{-3} m (0.25 inch) which was positioned at the same height as the sonic anemometer heart. The horizontal separation distance was 0.15 m between heart of the sonic anemometer and inlet tube. In addition, we used a membrane drier (Perma Pure) in order to dry the air before analyses. The flow and cell pressure were controlled with a needle valve at the inlet of the multi-pass cell. A vacuum pump (TriScoll 600, Varian Inc., USA) with a maximum volume flow rate of 400 L min^{-1} was located downstream of the multi-pass cell. The response time of the system was 0.08 s (Kroon et al., 2007). The Reynolds number in the tube was higher than 4000 (Kroon et al., 2007), which means a flow speed in the tube larger than 9.2 m s^{-1}. Furthermore, we calibrated the QCL spectrometer at least once a week using mixtures in N_2/O_2 of 1700 and 5100 ppb and 300 and 610 ppb (Scott Speciality Gases, the Netherlands). The sonic anemometer data and the QCL spectrometer output were logged using the RS232 output and processed using a data acquisition program developed at ECN, following the procedures of McMillen (1988). A more detailed explanation of this measurement set-up can be found in Kroon et al. (2007).

3.2. Methodology

The most widely accepted descriptions of atmospheric spectra and co-spectra available in the literature have been developed from data collected during the Kansas and Minnesota boundary-layer experiment (Kaimal et al., 1972). The empirical normalized spectrum $E_{ww}(f)$ for stable atmospheric conditions as given by Moore (1986) is

$$fE_{ww}(f) = \frac{f_{\text{nor}}}{A_{ww} + B_{ww} f_{\text{nor}}^{5/3}} \tag{4}$$

where w denotes the vertical wind velocity and f_{nor} denotes the normalized frequency which is given by

$$f_{\text{nor}} = \frac{fz}{U} \tag{5}$$

where f is the natural frequency and U the mean horizontal wind velocity, A_{ww} and B_{ww} are given by

$$\begin{aligned} A_{ww} &= 0.838 + 1.172\left(\frac{z}{L}\right) \\ B_{ww} &= 3.12 A_{ww}^{-2/3} \end{aligned} \tag{6}$$

for stable atmospheric conditions $z/L > 0$.

In this study, we validate the empirical spectra using LDA data. Determination of the spectra consists of two important steps. First, we generate the auto-correlation of the vertical velocity fluctua-

tion time series with the auto-correlation function defined by

$$\rho_{ww}(\tau) = \frac{R_{ww}(\tau)}{R_{ww}(0)} \tag{7}$$

where $R_{ww}(\tau)$ is the auto-covariance function which is given by

$$R_{ww}(\tau) = \overline{w'(t)w'(t+\tau)} \tag{8}$$

with t the time, τ the lag time and the over-bar denotes the expectation operator. Second, we determine the normalized spectral density function $E_{ww}(\omega)$ by the Fourier transform of $\rho(\tau)$, which reduces to a cosine transform since $\rho(\tau)$ is an even function

$$E_{ww}(\omega) = \frac{1}{2\pi}\int_{-\infty}^{\infty}\rho_{ww}(\tau)e^{-i\omega\tau}d\tau = \frac{1}{\pi}\int_{0}^{\infty}\rho_{ww}(\tau)\cos(\omega\tau)d\tau \tag{9}$$

where $\omega = 2\pi f$ is the radial frequency. The quantity $E_{ww}(\omega)d\omega$ can be interpreted as the fractional contribution to the power of the components with radial frequencies between ω and $\omega + d\omega$. We estimate the normalized spectral density $E_{ww}(\omega)$ using a variable window and the slotting technique with local normalization which is discussed in Tummers and Passchier (2001). We choose this technique because the LDA data are essentially non-equidistant.

A transformation from time domain to spatial domain is required to determine the one-dimensional turbulent energy spectrum $F_{ww}(k_1)$. In case of low turbulence intensity and an approximately stationary and homogeneous flow, Taylor's hypothesis of "frozen" turbulence can be invoked, which reads (e.g., Nieuwstadt, 1998)

$$\frac{\partial}{\partial t} \approx -U\frac{\partial}{\partial x} \tag{10}$$

where x is the coordinate aligned with the longitudinal wind velocity. Consequently, we can determine the one-dimensional turbulent energy spectrum $F_{ww}(k_1)$ by

$$\overline{w'^2} = 2\int_0^\infty F_{ww}(k_1)dk_1 = 2\int_0^\infty S_{ww}(\omega)d\omega \tag{11}$$

where k_1 is the wave number and $S_{ww}(\omega)$ is the unnormalized spectrum.

The smallest scale of turbulence is represented by the Kolmogorov scale η which is defined by (e.g., Nieuwstadt, 1998; Pope, 2000)

$$\eta = \left(\frac{\nu^3}{\varepsilon}\right)^{1/4} \tag{12}$$

where $\upsilon = 1.5 \times 10^{-5}\ \mathrm{m^2\ s^{-1}}$ denotes the kinematic viscosity of air and ε the dissipation rate. We estimate the dissipation rate using the Kolmogorov $-5/3$ law, which is valid in the inertial sub-range and is defined as (Nieuwstadt, 1998)

$$F_{ww}(k_1) = \alpha_w \varepsilon^{2/3} {k_1}^{-5/3} \tag{13}$$

in which α_w represents the Kolmogorov constant. The exact value of the Kolmogorov constant is uncertain, but we use 0.34 for the vertical one-dimensional turbulent energy spectrum (Högström, 1996).

We use the empirical normalized Kaimal co-spectrum $E_{wc}(f)$ for deriving the correction term χ_{high} for high frequency losses. Moore (1986) determined expressions for the normalized co-spectrum during stable ($z/L > 0$) and unstable atmospheric ($z/L < 0$) conditions based on the Kaimal co-spectra. During stable conditions the normalized co-spectrum is given by

$$fE_{wc}(f) = f\frac{C_{wc}(f)}{\overline{w'c'}} = \frac{f_{\mathrm{nor}}}{A_{wc} + B_{wc}{f_{\mathrm{nor}}}^{2.1}} \tag{14}$$

where $C_{wc}(f)$ is the unnormalized co-spectrum, and A_{wc} and B_{wc} are described by

$$\begin{aligned} A_{wc} &= 0.284\left(1 + 6.4\frac{z}{L}\right)^{0.75} \\ B_{wc} &= 2.34A_{wc}^{-1.1} \end{aligned} \tag{15}$$

and during unstable conditions

$$\begin{aligned} fE_{wc}(f) = f\frac{C_{wc}(f)}{\overline{w'c'}} &= \frac{12.92\,f_{\mathrm{nor}}}{(1+26.7\,f_{\mathrm{nor}})^{1.375}} \quad f_{\mathrm{nor}} < 0.54 \\ fE_{wc}(f) = f\frac{C_{wc}(f)}{\overline{w'c'}} &= \frac{4.378\,f_{\mathrm{nor}}}{(1+3.8\,f_{\mathrm{nor}})^{2.4}} \quad f_{\mathrm{nor}} \geq 0.54 \end{aligned} \tag{16}$$

The correction term χ_{high} for high frequency losses is calculated by

$$\chi_{\mathrm{high}} = \frac{\int_0^\infty C_{wc}(f)df}{\int_0^\infty T_{\mathrm{high}}(f)C_{wc}(f)df} \tag{17}$$

with $T_{\mathrm{high}}(f)$ the high frequency transfer function. In the literature, there are different derivations of the high transfer function $T_{\mathrm{high}}(f)$. For example: Moore (1986) stated that the transfer function is given by

$$T_{\mathrm{high}}^{\mathrm{Moore}}(f) = T_{wc}(f)\sqrt{T_{ww}(f)T_{cc}(f)} \tag{18}$$

which consists of three contributions, namely the transfer function acting on both parameters $T_{wc}(f)$, the transfer function acting only on the vertical wind velocity $T_{ww}(f)$ and the transfer function working only on the concentration measurement $T_{cc}(f)$. All three transfer functions can again be composed of several transfer functions. However, Horst (2000) contended that the transfer function for the covariance of w and c is not equal to the square root of the transfer function for both parameters. In this study, we show the impact of both strategies on the high frequency transfer function. In this evaluation, we include the transfer function for sensor separation $T_s(f)$, response time $T_r(f)$, tube damping $T_t(f)$ and path averaging $T_d(f)$. So, we do not take into account the effects of digital sampling since digital sampling has no effect on high frequency losses (Bosveld and Beljaars, 2001). The sensor separation transfer function is given by (Moore, 1986)

$$T_s(f_s) = \exp(-9.9\,{f_s}^{3/2}) \tag{19}$$

where $f_s = fs/U$ with s the separation distance, and the transfer function for limited response time is (e.g., Eugster and Senn, 1995; Horst, 1997)

$$T_r(f) = \frac{1}{1 + (2\pi f\tau_r)^2} \tag{20}$$

where τ_r is the response time of the QCL. Lenschow and Raupach (1991) give the transfer function for attenuation due to damping for a turbulent flow in the tube ($\mathrm{Re} > 2300$)

$$T_t(f_t) = \exp(-80Re^{-1/8}\,f_t^2) \tag{21}$$

in which $f_t = f(0.5DX)^{0.5}/u_t$ with D and X the tube diameter and length, and u_t the mean flow speed in the tube. In this analysis, we set the Reynolds number and mean flow speed to 4000 and 9.2 m s^{-1}. The transfer function $T_d(f)$ is dependent on the sonic anemometer configuration. Kristensen and Fitzjarrald (1984) have developed a method to estimate the transfer function $T_d(f)$ of a (1D or 3D) sonic anemometer with one vertical path. The sonic anemometers used in this study for EC flux measurements had three measurement paths which have a non-orthogonal orientation with an angle of 45° relative to the horizontal. Van Dijk (2001) derived the transfer function for this sonic anemometer configuration. We use Table 1 in Van Dijk (2001) for the transfer function $T_d(f)$.

In Fig. 3a, we plot the transfer functions $T_{high}(f)$ given by

$$T^1_{high}(f) = T_s(f)\sqrt{T_r(f)T_t(f)T_d(f)} \quad (22)$$

and by

$$T^2_{high}(f) = T_s(f)T_r(f)T_t(f)T_d(f) \quad (23)$$

together with the individual transfer functions $T_s(f)$, $T_r(f)$, $T_t(f)$ and $T_d(f)$ for a mean wind velocity of 1 m s^{-1}. It can be seen that the difference is small between both $T_{high}(f)$ transfer functions. For example: the frequency at which the attenuation is 10% is about 0.29 and 0.27 Hz for $T^1_{high}(f)$ and $T^2_{high}(f)$, respectively. In addition, it is shown that the transfer function for sensor separation and response time are much more important than the transfer function for tube attenuation and path averaging. However, the transfer functions of sensor separation and path averaging are dependent on the mean wind velocity. Therefore, we investigate further the influence of the individual transfer functions on the total transfer function using $f_{90\%}$ which is defined as the frequency at which the attenuation is 10%. We illustrate $f_{90\%}$ for each transfer function as function of the mean wind velocity in Fig. 3b. We show that for wind velocities smaller than 1 m s^{-1} the total transfer function $T_{high}(f)$ is mainly dominated by the transfer function for sensor separation $T_s(f)$ and for wind velocities larger than 3 m s^{-1} by the transfer function for limited response time of the QCL $T_r(f)$. The $f_{90\%}$ is approximately equal to $0.045U/s$ for $T_s(f)$ (Moore, 1986), 0.65 Hz for $T_r(f)$, 1.98 Hz for $T_t(f)$ and $0.29U/d$ for $T_d(f)$ (Van Dijk, 2001). Thus, the influence of $T_t(f)$ and $T_d(f)$ is much smaller on the high frequency transfer function $T_{high}(f)$ than the influence of $T_s(f)$ and $T_d(f)$, therefore, we neglect the transfer functions of $T_t(f)$ and $T_d(f)$ in this study. In addition, Kristensen et al. (1997) derived that the attenuation due to sensor separation could be reduced by placing the inlet tube below the sonic anemometer heart. We recommend installing the inlet tube at that location in future measurements. Performing the analyses using the strategy of Horst (2000) and retaining only transfer functions for sensor separation and QCL-response, we have

$$T_{high}(f) = T_s(f)T_r(f). \quad (24)$$

The co-spectra of EC fluxes are dependent on the measurement height, mean wind velocity and the stability (Eqs. (14)–(16)). To illustrate the co-spectral behavior, we plot them for several stable conditions (Fig. 4a). In addition, we calculate the correction term χ_{high} for high frequency losses using Eq. (17) taking an averaging time T = 30 min, a measurement height z = 3 m and a Kolmogorov scale $\eta = 1.0\times10^{-3}$ m. In Fig. 4b, it is shown that the correction term is also dependent on the wind velocity and the stability. The correction term is larger than 1.10 for mean wind velocities larger than 3 m s^{-1} and stabilities z/L larger than 0.1. This in agreement with the simple formula derived in Horst (1997). Therefore, it is very important to correct for high frequency losses during stable conditions.

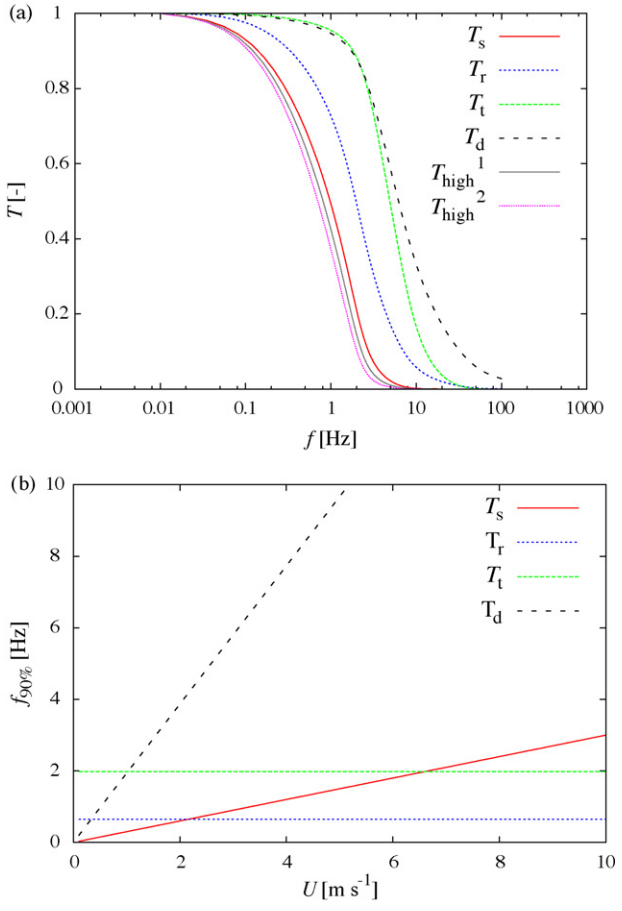

Fig. 3. (a) The transfer functions for high frequency losses by EC flux measurements at a mean wind speed of 1 m s^{-1} where $T^1_{high}(f) = T_s(f)\sqrt{T_r(f)T_t(f)T_d(f)}$ and $T^2_{high}(f) = T_s(f)T_r(f)T_t(f)T_d(f)$ with $T_s(f)$, $T_r(f)$, $T_t(f)$ and $T_d(f)$ the transfer function for sensor separation, limited response time of the QCL, damping effects by the tube and path averaging over the sonic anemometer path, respectively. (b) The frequency $f_{90\%}$ of all individual transfer function as function of mean wind velocity in which $f_{90\%}$ gives the frequency on which 90% of the contributions in unaffected.

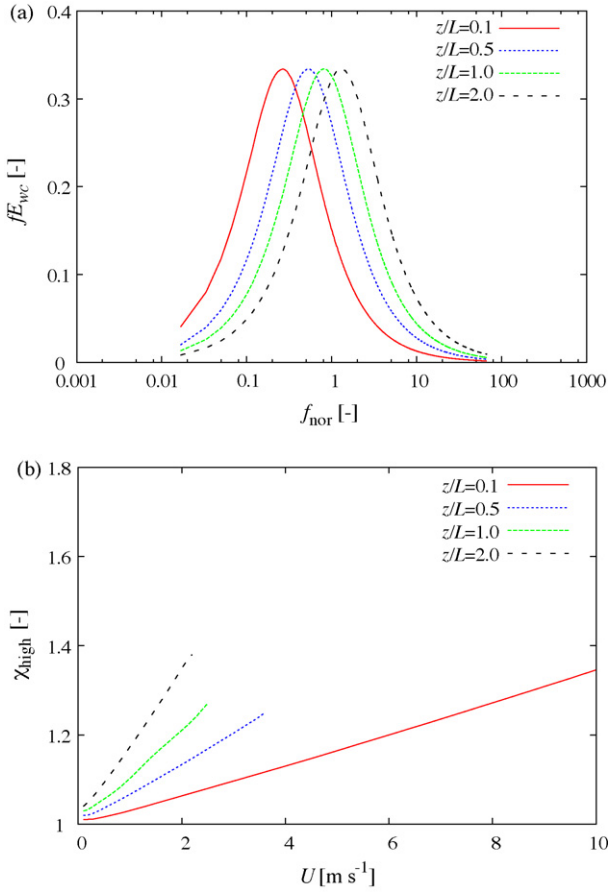

Fig. 4. (a) Normalized Kaimal co-spectrum E_{wc} for several stable atmospheric conditions and (b) the correction term χ_{high} for high frequency losses for the wind velocity and z/L range at 3 m height at Oukoop in the Netherlands.

The high frequency corrected EC flux EC_{wc} is given by

$$EC_{wc} = \chi_{high} EC_{wc}^{cal.} \quad (25)$$

where $EC_{wc}^{cal.}$ is the EC flux which has been corrected already for calibrations. We derive the uncorrected EC fluxes EC_{wc}^{meas} using different phases. First, we analyze visually the raw data of vertical wind velocity $w(t)$ in m s^{-1} and gas concentration of CH_4 and N_2O $c(t)$ in ppb for unrealistic spikes and possible effects of equipment malfunctioning. Next, we determine the time average of w and c using a running mean operation which is defined by (Lee et al., 2004)

$$\tilde{w}_k = \left(1 - \frac{\Delta t}{\tau_f}\right)\tilde{w}_{k-1} + \frac{\Delta t}{\tau_f} w_k$$
$$\tilde{c}_k = \left(1 - \frac{\Delta t}{\tau_f}\right)\tilde{c}_{k-1} + \frac{\Delta t}{\tau_f} c_k \quad (26)$$

where Δt is the interval between two samples, τ_f is the running mean filter constant and the subscript k refers to the k-th sample. A running mean filter is a practical solution to filter laser drift contributions which occur due to interference fringes in the optical system and small movements of the fringes due to temperature and pressure effects. The laser drift contributions behave like additional noise on the signal which can lead to a higher detection limit. The running mean filter constant is set to the time scale on which laser drift starts, which has been determined using an Allan Variance analysis (Kroon et al., 2007). This filter could cause an under- or overestimation of the flux due to filtering of large eddy contributions. The amount of underestimation is dependent on the stability of the atmosphere, the mean wind velocity, the measurement height and the running mean filter time constant. We calculate the co-variances using a 120 s running mean filter constant and a 30 min averaging time with

$$cov_{wc} = \overline{w'c'} = \frac{1}{n_s}\sum_{k=1}^{n_s}(w_k - \tilde{w}_k)(c_k - \tilde{c}_k) \quad (27)$$

where n_s is the number of samples in the averaging period. Kroon et al. (2009) show that the effect of a running mean filter is mostly small for this specific measurement set-up. Furthermore, we determine the time lag between the sonic anemometer and the QCL spectrometer data caused by the travel time of the air through the sampling tube using the covariance as function of the delay time, which is given by

$$EC_{wc}^{meas} = cov_{wc}(n\Delta t) = \frac{1}{n_s}\sum_{k=1}^{n_s} w'_k c'_{k+n\Delta t}. \quad (28)$$

We assume that the EC flux EC_{wc}^{meas} is the value at the delay time when the absolute value of the covariance reaches its maximum.

The expression for the net ecosystem exchange of CH_4 (F_{wCH_4}) and N_2O (F_{wN_2O}) is derived by the tracer conservation equation (e.g. Aubinet et al., 2000). Assuming horizontal homogeneity and a flat terrain within the averaging time of 30 min, the net ecosystem exchange F_{wc} consists of two contributions, the storage change term St_c and the eddy covariance flux term EC_{wc}, and is given by

$$F_{wc} = \underbrace{\frac{\bar{c}_i - \bar{c}_{i-1}}{T_{av}} h}_{St_c} + \underbrace{\overline{w'c'}|_{z=h}}_{EC_{wc}} \quad (29)$$

where h is the measurement height in m, i the flux number and T_{av} the averaging time in s. The storage change term St_c is calculated using the average values of CH_4 and N_2O at 3 m height over each 30 min period. Moreover, we flag the F_{wc} using the in-stationary test of Foken and Wichura (1996) and we check the fetch by a footprint model based on the Kormann–Meixner method (Kormann and Meixner, 2001; Neftel et al., 2007). By means of that, we reject the 30 min F_{wc} value with flags larger than 2 and when less than 70% of the flux came from the dairy farm site. We convert the remaining fluxes from ppb m s^{-1} to ng C m^{-2} s^{-1} and ng N m^{-2} s^{-1} using the ideal gas law for CH_4 and N_2O, respectively.

4. Results

We have designed an LDA set-up suitable for atmospheric measurements and have employed it during five measurement nights at Cabauw in 2008. The mean sampling frequency was 354, 163, 527, 144 and 62 Hz on 8 February, 13 February, 7 April, 17 June and 18 June 2008, respectively. The total measurement time varied from about 1 h to three and a half hours. The dataset of each night consisted of several recorded files with a maximum of data points of 1×10^5 each. We checked the quality of individual files visually using vertical velocity time series and auto-correlation plots. We rejected files from the dataset when the auto-correlation function differed drastically from 1 at time $t = \Delta\tau$ which indicated an unacceptable noise contribution to the signal.

We derived the variance spectra over one night using all the accepted recorded LDA files during that night, and used the same time periods for the analysis of the sonic anemometer data. Using these data, we determined normalized spectral density $E_{ww}(f)$, for both LDA and sonic anemometry using Eq. (9) over a frequency range from 2×10^{-3} to 477 Hz. However, the maximum detected frequencies, from which the contributions are well measured, are much lower than 477 Hz. We set the maximum frequency to $f_{max}^{Sonic} = U/\pi d$ for sonic anemometry

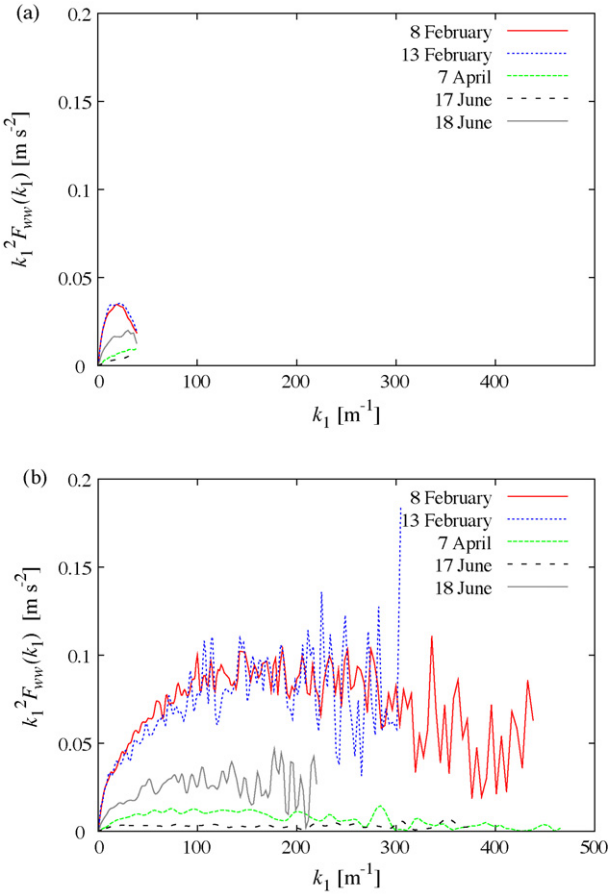

Fig. 5. (a) One-dimensional spectrum $k_1^2 F_{ww}(k_1)$ measured by sonic anemometry and (b) LDA at 1 m height at Cabauw in the Netherlands during five nights in 2008.

Table 2
Overview of spectral parameters for five measurement nights at Cabauw in the Netherlands in 2008.

	8 February	13 February	7 April	17 June	18 June
U_{1m} (m s^{-1})	1.82	1.64	0.64	0.49	1.12
σ_{ww}^2 (m^2 s^{-2})	0.036	0.039	0.003	0.002	0.013
ε (m^2 s^{-3})	0.0041	0.0035	0.0003	0.0001	0.0009
f_{max}^{Sonic} (Hz)	12	10	4	3	7
f_{max}^{LDA} (Hz)	130	81	49	30	40
η (m)	1×10^{-3}	1×10^{-3}	2×10^{-3}	2×10^{-3}	1×10^{-3}
λ_ε (m)	19×10^{-3}	20×10^{-3}	37×10^{-3}	48×10^{-3}	28×10^{-3}
λ_{min}^{Sonic} (m)	157×10^{-3}	157×10^{-3}	157×10^{-3}	157×10^{-3}	157×10^{-3}
λ_{min}^{LDA} (m)	14×10^{-3}	20×10^{-3}	13×10^{-3}	16×10^{-3}	28×10^{-3}
$\lambda_w^{prod\,a}$ (m)	1.78	NA[c]	0.97	0.73	1.53
$\lambda_w^{prod\,b}$ (m)	1.32	2.83	0.49	0.40	1.06

[a] Measured by the profile method using 2 and 10 m data.
[b] Measured by the EC flux method at 3 m height.
[c] The production scale could not be determined by Osvaldo et al. (1987) since this algorithm is only valid during for $z/L > 0$.

and to the maximum valid frequency of the normalized spectral density $E_{ww}(f)$ for LDA. The maximum frequency ranges from 3 to 12 Hz for sonic anemometry and from 30 to 130 Hz for LDA. In addition, we calculate the one-dimensional spectrum $F_{ww}(k_1)$ using Eqs. (10) and (11). Since, the spectra of the sonic anemometer are derived using an equidistant dataset, the area below $F_{ww}(k_1)$ versus k_1 plot on linear scale indicates approximately the average σ_{ww}^2 during the whole period.

However, the LDA spectra are derived from non-equidistant datasets which cause an error to the average variance σ_{ww}^2. The time periods with a higher sampling frequency have more weight on the average variance. Therefore, the area below $F_{ww}(k_1)$ versus k_1 plot on linear scale does not exactly indicate the average σ_{ww}^2 during the whole period. Still we use σ_{ww}^2 measured by LDA since the present research questions do not involve the magnitude of w-variance.

We emphasize the difference in detected frequency range using plots of the one-dimensional w-dissipation spectrum $k_1{}^2F_{ww}(k_1)$ (Fig. 5). It reveals that much smaller scales (higher wave numbers) can be detected with LDA. In addition, the

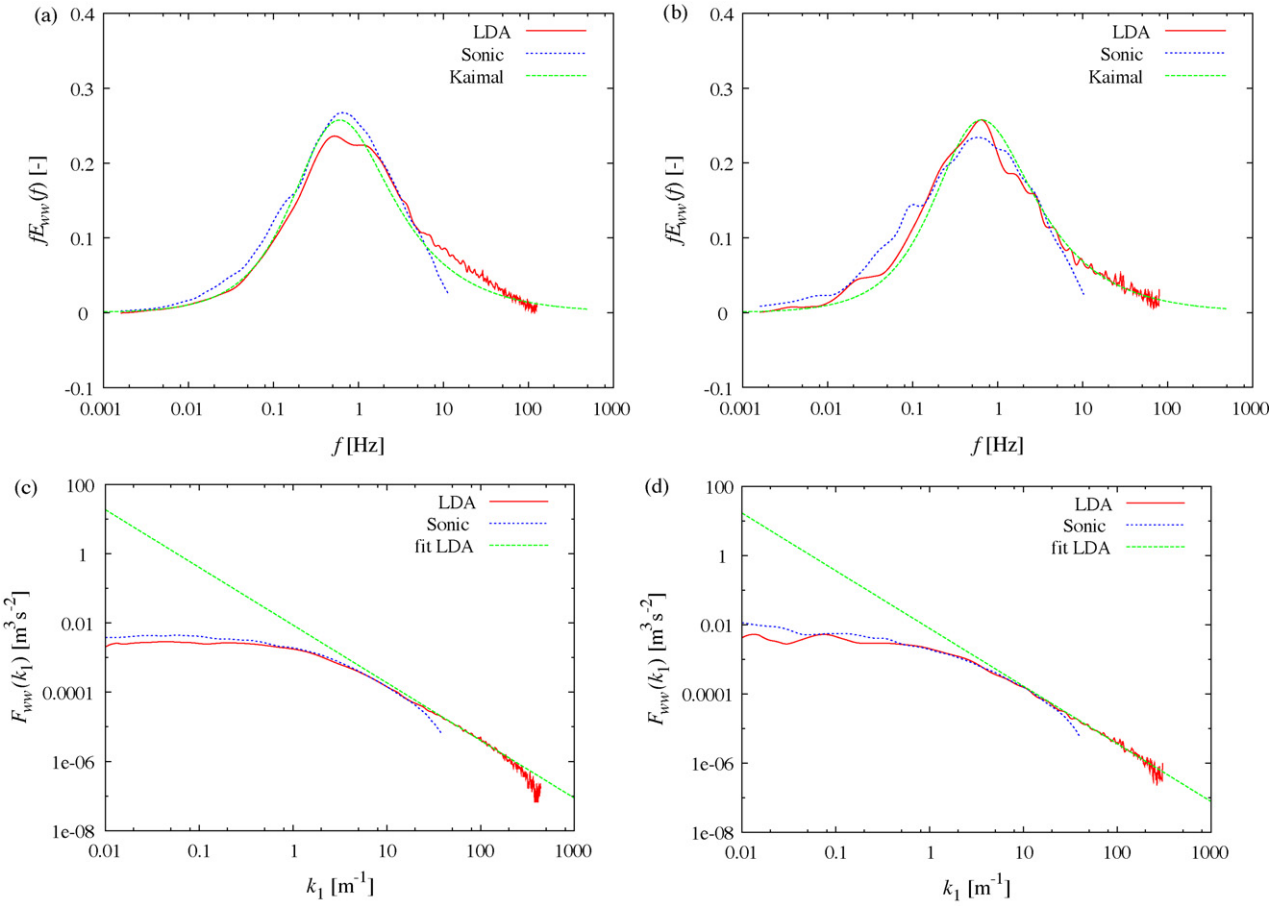

Fig. 6. (a, b) LDA, sonic anemometry normalized $fE_{ww}(f)$ spectrum and Kaimal spectrum on semi-log scale of 8 February 2008 and 13 February 2008. (c, d) One-dimensional spectrum $k_1F_{ww}(k_1)$ of 8 February 2008 and 13 February 2008 on double-log scale measured by LDA and sonic anemometry, and the fitted line to the LDA spectra between k_1 = 37 m^{-1} and k_1 = 105 m^{-1}.

attenuation effects in the sonic spectra are already visible for frequencies smaller than $f_{\max}^{\text{Sonic}}$.

We investigated the validity of the spectral −5/3 shape of the Kaimal spectrum over the spectral range using LDA data which consists of contributing eddies much smaller than the smallest detected scale by the sonic anemometer (about 157×10^{-3} m). We validate the spectral shape in the inertial sub-range using the average vertical wind velocity spectrum over each night which is schematically given by

$$\overline{F_{ww}}(k_1) = \frac{1}{N_{250s}} \sum_{n=1}^{N_{250s}} \alpha_w \varepsilon^{2/3} k_1^b \tag{30}$$

with N_{250s} the number of 250 s slots and b the power law exponent. Since, the meteorological parameters, e.g., mean horizontal wind velocity and Monin–Obukhov length scale, varied during these nights, the expected production scale, i.e., starting point of the inertial sub-range varied as well. The power law exponent b can only be derived correctly for high frequencies, which means high wave numbers, for which all individual 250 s spectrum are in the inertial sub-range. The inertial sub-range ranges from l_{EI} to l_{DI} with $l_{\text{EI}} \approx l_{\text{O}}/6$ and $l_{\text{DI}} \approx 60\eta$ where l_{O} represents the production scale (Pope, 2000). We estimated the production scale λ_w^{prod} by (Osvaldo et al., 1987)

$$\lambda_w^{\text{prod}} = \frac{z}{\left[0.50 + 1.252(z/L)^{3/5}\right]^{3/2}} \tag{31}$$

for each night and found that the smallest production scale was 0.73 m using the profile method (Table 2). We estimate the Kolmogorov scale at 1×10^{-3} m.

To avoid a large uncertainty in the estimation of b according to a small number of data points within the fit-range, we set the range from 0.17 to 0.06 m (k_1 = 37–105 m^{-1}) which leads to N = 80 data points in each night. We fit the function

$$f(x) = a + bx \tag{32}$$

to $\log(F_{ww})$ with $x = \log(k_1)$ with fitting parameters a and b. The exponent b is estimated to be −1.81 with an uncertainty $2\sigma_b/\sqrt{80}$ of 0.41. As a result, the shape of the inertial sub-range is in agreement with the Kolmogorov −5/3 law and thus with the Kaimal spectra (Fig. 6a and b). The stable and very stable conditions do not lead to a significant change in spectral behavior at high frequencies within the sub-range; see for example the one-dimensional spectra of 8 and 13 February 2008 measured by LDA and sonic anemometry in Fig. 6c and d.

To answer the question whether LDA was capable of measuring the spectra all the way down to the dissipation scale, it is important to emphasize the distinction between the Kolmogorov scale η (defined in Eq. (12)), and the "dissipation scale" $\lambda_\varepsilon = 2\pi/k_\varepsilon$.We define the latter as the scale at which most of the dissipation takes place, which can be found by locating the peak k_ε in the graph[1] of ${k_1}^3 F_{ww}(k_1)$ versus $\log(k_1)$. The dissipation scale will be proportional to the Kolmogorov scale, i.e., $\lambda_\varepsilon = \gamma\eta$, but the relevant point to be made here is that the dimensionless factor γ can actually be quite large. In Appendix A, we show analytically that γ can be as large as 20.

For each experiment, we determine the Kolmogorov scale using Eqs. (12) and (13) where we estimate the dissipation rate ε by fitting Eq. (13) through the measured spectra $\overline{F_{ww}}(k_1)$ from k_1 = 37 to 105 m^{-1} (Fig. 6c and d). The Kolmogorov scale η ranges from 1.0×10^{-3} to 2.4×10^{-3} m. Therefore, the expected dissipation scale λ_ε varies from 19×10^{-3} to 48×10^{-3} m. This

[1] The reason for having k^3 rather than k^2 arises from the fact that the spectral densities are evaluated on a logarithmic k-axis, yielding the additional factor k, since $\mathrm{d}k = k\mathrm{d}\log(k)$.

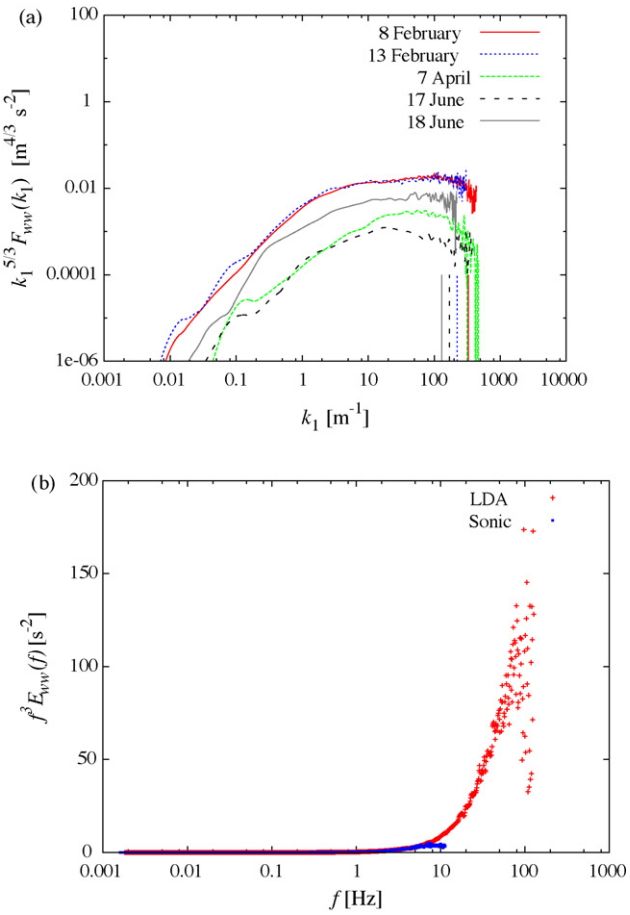

Fig. 7. (a) The unnormalized ${k_1}^{5/3} F_{ww}(k_1)$ spectrum measured at Cabauw in the Netherlands during five nights in 2008, the vertical lines show an indication of the dissipation scale which is given by the peak in the $f^3 E_{ww}(f)$ spectrum. (b) The normalized $f^3 E_{ww}(f)$ spectrum at 8 February 2008.

shows that the dissipation scale is resolved during all nights (Fig. 7a). As an example, we plot the normalized spectrum $f^3 E_{ww}(f)$ of 8 February 2008 in Fig. 7b. A clear peak is detected, which confirms that the dissipation range is resolved by the LDA measurements. A summary of all used spectral parameters is given in Table 2.

Thus, the −5/3 shape is found to be valid down to the dissipation scale during (strongly) stratified conditions; the shape of the empirical Kaimal spectrum is therefore valid as well. Because we anticipated the biggest influence of stratification on the w-spectra (through the direct action of buoyancy), we now explicitly assume that the Kaimal co-spectra are valid as well. If there are no turbulent contributions anymore at a certain scale in the vertical wind velocity spectrum then there are also no turbulent contributions anymore in $C_{wc}(f)$. Hence, we assume that the EC fluxes $\text{EC}_{wc}^{\text{cal.}}$ can be corrected for the small-scale non-detected eddies using Eq. (17). The correction term χ_{high} is based on integrating the empirical Kaimal co-spectrum and transfer function over a frequency range. We compare three correction algorithms based on different frequency ranges. All algorithms start at a frequency of 5.6×10^{-4} Hz and they end at different frequencies, namely at the cut-off frequency of the Ogive analyses in Kroon et al. (2007) (2 Hz), the Nyquist frequency (10 Hz) and at the frequency corresponding to the end of the inertial sub-range ($f = U/l_{\text{DI}} = U/60\eta$).

We use 1 month EC flux data of CH_4 and N_2O measured by QCL spectrometry at Reeuwijk in the Netherlands from 14 September

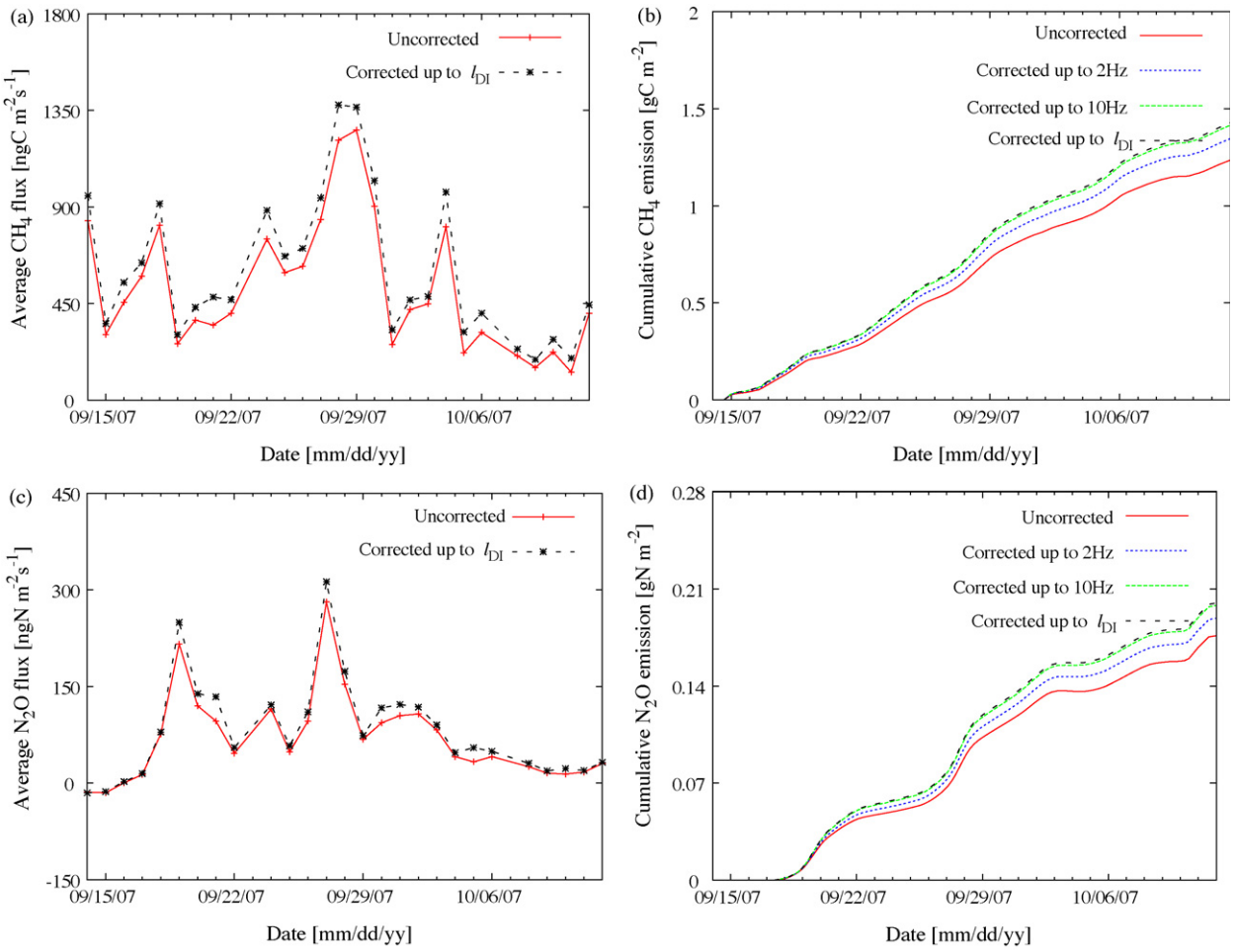

Fig. 8. (a, c) CH_4 and N_2O daily average fluxes and (b, d) cumulative emissions for different high frequency correction algorithms measured at Oukoop in the Netherlands from 14 September 2007 to 12 October 2007. Corrected up to l_{DI} denotes a frequency correction up to the end of the inertial sub-range.

to 12 October 2007. We rejected non-steady state 30 min fluxes and 30 min fluxes corresponding to z/L values larger than 10. Finally, we calculate the average correction factors over $N = 819$ and $N = 884$ EC fluxes for CH_4 and N_2O, respectively. For CH_4 the average correction factor and its uncertainty lead to 1.10 (±0.01), 1.17 (±0.01) and 1.18 (±0.01) for correcting until 2, 10 Hz and the frequency corresponding to l_{DI}, respectively. And for N_2O the average correction factor and its uncertainty lead to 1.10 (±0.01), 1.16 (±0.01) and 1.17 (±0.01), respectively. We give the mean wind velocity and stability parameter over $N = 819$ CH_4 fluxes, however, they are close to the values over $N = 884$ N_2O fluxes. The mean wind velocity ranges from 0.2 to 8.0 m s^{-1} with an average and standard deviation of about 2.2 and 1.7 m s^{-1}. The stability parameter z/L ranges from −0.2 to 9.4 with an average and standard deviation of 0.3 and 0.9.

We illustrate the effect of the high frequency correction on daily averages of F_{wc} (Eq. (29)) for this specific measurement set-up. In addition, in Fig. 8 we show the cumulative emissions for the uncorrected and the three correction algorithms over 1 month. The average daily CH_4 and N_2O emissions are 557 ng C m^{-2} s^{-1} and 70 ng N m^{-2} s^{-1} for the uncorrected algorithm, and 666 ng C m^{-2} s^{-1} and 81 ng N m^{-2} s^{-1} for the corrected algorithm until the frequency corresponding to l_{DI}. The cumulative CH_4 emissions over this month are 1.246, 1.358, 1.428 and 1.441 g C m^{-2}, and the cumulative N_2O emissions are 0.177, 0.189, 0.199 and 0.200 g N m^{-2} for the uncorrected, corrected until 2 Hz, corrected until 10 Hz and corrected until the frequency corresponding to l_{DI}, respectively. Thus, the cumulative emissions are about 15% larger with high frequency corrections until l_{DI}, which reveals the importance of correcting for the non-detected eddies. There is only a small difference between the correction until the Nyquist frequency and the correction until the end of the inertial sub-range l_{DI}. However, there is a significant difference between the correction until 2 Hz and the Nyquist frequency. Therefore, we recommend including high frequency losses at least until the Nyquist frequency.

In addition, we independently check the reliability of the high frequency correction. To this end we compare the EC flux measurements with static chambers at the same measurement site. In Schrier-Uijl et al. (submitted for publication), it has been shown that over a 3 months period the cumulative emissions of CH_4 fluxes measured by the EC flux technique were about 17% lower than with static chambers. In that study, the high frequency correction has not been taken into account. However, in Kroon et al. (submitted for publication), the annual CH_4 balances were compared of both measurement techniques over the years 2006, 2007 and 2008 and the high frequency correction has been applied on the EC flux measurements. The average annual CH_4 balance was estimated at 165 and 170 kg CH_4 ha^{-1} yr^{-1} for the EC flux and static chamber method, respectively. Consequently, the difference between both methods decreased significantly when the correction was applied.

5. Conclusions

We have developed an LDA system that was capable of operating under atmospheric conditions. The developed LDA system was compact and made use of a diode pumped solid-state laser which did not need a high power voltage and water-cooling. External particles were entrained in the flow since ambient aerosols were not enough to perform the measurements. Tracer particles were produced by a smoke generator using a fluid based water and glycol. The seeding particles were injected into the atmospheric flow at a distance of about 25 m upstream of the measurement location using either a 20 or a 60 m long circular segment.

We carried out the LDA measurements at 1 m height at Cabauw in the Netherlands during five nights in the period from February to July 2008. Much smaller scales were detected using LDA than by sonic anemometry during all five measurement nights, with scales ranging from 40 to 130 Hz with LDA and from 4 to 12 Hz with sonic anemometry. The LDA measurements were found to be able to resolve the vertical wind velocity spectra down to the scale at which most dissipation takes place.

With the LDA data we were able to validate the spectral shape of the high frequency range of the empirical Kaimal spectrum during stable conditions. This evaluation was limited to the vertical wind velocity spectrum since our LDA set-up was limited to one wind-component and no techniques appeared available to sample, e.g., CH_4 and N_2O up to the dissipation scale. The inertial sub-range of the LDA spectra was in good agreement with the $-5/3$ Kolmogorov law and therefore with the empirical Kaimal spectra. Making the explicit assumption that the Kaimal co-spectra were valid as well, we subsequently assessed the impact of high frequency corrections. The effects of the various high frequency correction algorithms were analyzed using 1 month of eddy covariance flux data of CH_4 and N_2O measured by QCL spectrometry at Reeuwijk in the Netherlands. After correction, the cumulative emissions increased by about 15% for both gases. This reveals the importance of correcting for high frequency losses.

Acknowledgements

This research was part of the Dutch National Research Program BSIK ME1. Thanks are due to our colleagues H. van't Veen and A. Vermeulen from ECN for their contributions to the Reeuwijk measurements. We are very grateful to M. Brinkenberg, C. van Oort, J. Warmer from KNMI and E. de Beus, H. Ouwersloot, R. Rodink, S. de Roode and P. Verhagen from TU Delft for their assistance during the measurements at Cabauw. Finally, we owe a special debt of gratitude to the farmer T. van Eijk and to the KNMI for using their sites.

Appendix A

As mentioned in Section 4, there is a distinction between the Kolmogorov scale $\boldsymbol{\eta} = (\boldsymbol{\upsilon}^3/\boldsymbol{\varepsilon})^{1/4}$ and the actual scale $\boldsymbol{\lambda}_{\boldsymbol{\varepsilon}}$ where the dissipation is maximal. This scale can be extracted from the dissipation spectrum by locating the peak k_ε. This amounts to locating the peak in the graph of $k^3E(k)$ when plotted as a function of $\log(k)$ ('scale' is a logarithmic concept). The purpose of this appendix is to get an estimate for the value of the proportionality constant $\boldsymbol{\gamma} = \boldsymbol{\lambda}_{\boldsymbol{\varepsilon}}/\boldsymbol{\eta}$ using a model spectrum of turbulence that includes the dissipation range. Such a model was suggested by, e.g., Pope (2000) and reads

$$E(k) = C\varepsilon^{2/3}k^{-5/3} f_L(kL) f_\eta(k\eta) \tag{A.33}$$

with

$$f_L(kL) = \left(\frac{kL}{((kL)^2 + c_L)^{1/2}}\right)^{5/3+p_0},$$
$$f_\eta(k\eta) = \exp(-\beta(((k\eta)^4 + c_\eta^4)^{1/4} - c_\eta). \tag{A.34}$$

The parameters are set to $C = 1.5$, $\boldsymbol{\beta} = 5.2$, $c_L = 6.78$, $c_\eta = 0.466$, $p_0 = 2.0$ and the constant c_η is determined by the requirement that $2\boldsymbol{\nu}k^2E(k)$ integrate to $\boldsymbol{\varepsilon}$. We derive the one-dimensional spectrum $F_{uu}(k_1)$ and $F_{ww}(k_1)$ using (Pope, 2000)

$$F_{ww}(k_1) = \frac{1}{4}\left(F_{uu}(k_1) - k_1\frac{dF_{uu}(k_1)}{dk_1}\right),$$
$$F_{uu}(k_1) = \frac{1}{2}\int_{k_1}^{\infty}\frac{E(k)}{k}\left(1 - \frac{k_1^2}{k^2}\right)dk. \tag{A.35}$$

We plot $k_1F_{ww}(k_1)$ and $k_1{}^3F_{ww}(k_1)$ in Fig. A.1 for two different dissipation rates. Location of the peak k_ε enables one to find the factor

$$\gamma = \frac{\lambda_\varepsilon}{\eta} = \frac{2\pi}{\eta k_\varepsilon}. \tag{A.36}$$

In this way, we derive that the factor $\boldsymbol{\gamma}$ is equal to 15, 25 and 20 for the $E(k)$, $F_{uu}(k_1)$ and $F_{ww}(k_1)$, respectively.

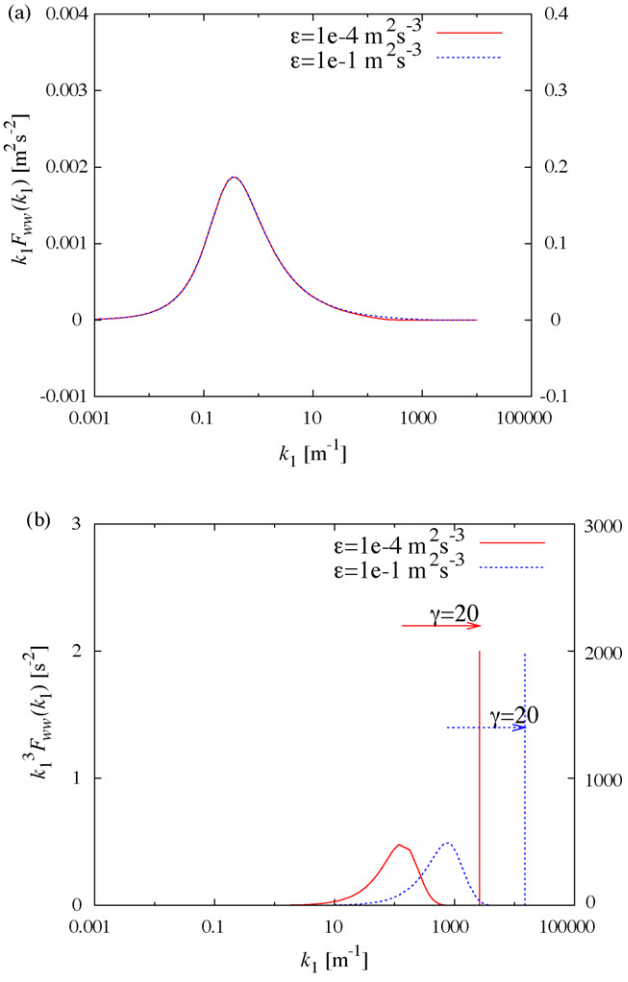

Fig. A.1. (a) The model $k_1F_{ww}(k_1)$ and (b) $k_1{}^3F_{ww}(k_1)$ spectra for two dissipation rates given by Pope (2000) and vertical lines which indicate the Kolmogorov scale. The factor γ is given, which defines the ratio between the Kolmogorov scale and the scale at which the dissipation peaks.

References

Absil, L.H.J., 1995. Analysis of the laser Doppler measurement technique for application in turbulent flows. PhD thesis. Delft University of Technology, The Netherlands.

Ammann, C., Brunner, A., Spirig, C., Neftel, A., 2006. Technical note: water vapour concentration and flux measurements with PTR-MS. Atmospheric Chemistry and Physics 6, 4643–4651.

Aubinet, M., Grelle, A., Ibrom, A., Rannik, Ü., Moncrieff, J., Foken, T., Kowalski, A.S., Martin, P.H., Berbigier, P., Bernhoffer, C., Clement, R., Elbers, J., Granier, A., Grünwald, T., Morgenstern, K., Pilegaard, K., Rebmann, C., Snijders, W., Valentini, R., Vesala, T., 2000. Estimates of the annual net carbon and water exchange of forests: the EUROFLUX methodology. Advances in Ecological Research 30, 113–175.

Beljaars, A.C.M., Bosveld, F.C., 1997. Cabauw data for the validation of land surface parameterization schemes. Journal of Climate 10, 1172–1193.

Bosveld, F.C., 1999. The KNMI Garderen experiment: micro-meteorological observations 1988–1989 corrections. KNMI Scientific Report, WR 99-03.

Bosveld, F.C., Beljaars, A.C.M., 2001. The impact of sampling rate on eddy-covariance flux estimates. Agricultural and Forest Meteorology 109, 39–45.

Eugster, W., Senn, W., 1995. A cospectral correction model for measurement of turbulent NO_2 flux. Boundary-Layer Meteorology 74, 321–340.

Foken, T., Wichura, B., 1996. Tools for quality assessment of surface-based flux measurements. Agricultural and Forest Meteorology 78, 83–105.

Fowler, D., Hargreaves, K.J., Skiba, U., Milne, R., Zahniser, M.S., Moncrieff, J.B., Beverland, I.J., Gallagher, M.W., 1995. Measurements of CH_4 and N_2O fluxes at the landscape scale using micrometeorological methods. Philosophical transactions of the Royal Society of London A 351, 339–356.

Gulitski, G., Kholmyansky, M., Kinzelbach, W., Lüthi, B., Tsinober, A., Yorish, S., 2007. Velocity and temperature derivatives in high-Reynolds-number turbulent flows in the atmospheric surface layer. Part 1. Facilities, methods and some general results. Journal of Fluid Mechanics 589, 57–81.

Hendriks, D.M.D., Dolman, A.J., Molen Van der, M.K., Huissteden, J., 2008. A compact and stable eddy covariance set-up for methane measurements using off-axis integrated cavity output spectroscopy. Atmospheric Chemistry and Physics 8, 431–443.

Högström, U., 1996. Review of some basic characteristics of the atmospheric surface layer. Boundary-Layer Meteorology 78, 215–246.

Horst, T.W., 1997. A simple formula for attenuation of eddy fluxes measured with first-order-response scalar sensor. Boundary-Layer Meteorology 82, 219–233.

Horst, T.W., 2000. On frequency response corrections for eddy covariance flux measurements. Boundary-Layer Meteorology 94, 517–520.

Kaimal, J.C., Wyngaard, J.C., Izumi, Y., Coté, O.R., 1972. Spectral characteristics of surface-layer turbulence. Quarterly Journal of the Royal Meteorological Society 98, 563–589.

Kormann, R., Meixner, F.X., 2001. An analytical footprint model for non-neutral stratification. Boundary-Layer Meteorology 99, 207–224.

Kraan, C., Oost, W.A., 1988. A new way of anemometer calibration and its application to a sonic anemometer. Journal of Atmospheric and Oceanic Technology 6, 516–524.

Kristensen, L., Fitzjarrald, D.R., 1984. The effect of line averaging on scalar flux measurements with a sonic anemometer near the surface. Journal of Atmospheric and Oceanic Technology 1, 138–146.

Kristensen, L., Mann, J., Oncley, S.P., Wyngaard, J.C., 1997. How close is close enough when measuring scalar fluxes with displaced sensors? Journal of Atmospheric and Oceanic Technology 14, 814–821.

Kroon, P.S., 2004. De sluiting van de oppervlakte energiebalans gedurende tebex (1995–1996). KNMI Technical Report, TR-261 (in Dutch).

Kroon, P.S., Hensen, A., Jonker, H.J.J., Zahniser, M.S., Van 't Veen, W.H., Vermeulen, A.T., 2007. Suitability of quantum cascade spectroscopy for CH_4 and N_2O eddy covariance flux measurements. Biogeosciences 4, 715–728.

Kroon, P.S., Hensen, A., Jonker, H.J.J., Ouwersloot, H.G., Vermeulen, A.T., Bosveld, F.C., 2009. Uncertainties in eddy covariance flux measurements assessed from CH_4 and N_2O observations, Agricultural and Forest Meteorology, doi:10.1016/j.agrformet.2009.08.008.

Kroon, P.S., Schrier-Uijl, A.P., Hensen, A., Veenendaal, E.M., Jonker, H.J.J. Annual balances of CH_4 and N_2O from a managed fen meadow using eddy covariance flux measurements, European Journal of Soil Science, submitted for publication.

Laville, P., Jambert, C., Cellier, P., Delmas, R., 1999. Nitrous oxide fluxes from a fertilized maize crop using micrometeorological and chamber methods. Agricultural and Forest Meteorology 96, 19–38.

Lee, X.L., Massmann, W., Law, B., 2004. Handbook of Micrometeorology. Kluwer Academic Publishers, Dordrecht, the Netherlands.

Lenschow, D.H., Raupach, M.R., 1991. The attenuation of fluctuations in scalar concentrations through sampling tubes. Journal of Geophysical Research 96 (D8), 15259–15268.

McMillen, R.T., 1988. An eddy correlation technique with extended applicability to non-simple terrain. Boundary-Layer Meteorology 43, 231–245.

Moore, C.J., 1986. Frequency response corrections for eddy correlation systems. Boundary-Layer Meteorology 37, 17–35.

Neftel, A., Flechard, C., Ammann, C., Conen, F., Emmenegger, L., Zeyer, K., 2007. Experimental assessment of N_2O background fluxes in grassland systems. Tellus B 59, 470–482.

Nieuwstadt, F.T.M., 1998. Turbulentie. Epsilon Uitgaven, Utrecht, the Netherlands.

Osvaldo, L., Moreas, L., Epstein, M., 1987. The velocity spectra in the stable surface layer. Boundary-Layer Meteorology 40, 407–414.

Pope, S.B., 2000. Turbulent Flows. Cambridge University Press, UK.

Schotanus, P., Nieuwstadt, F.T.M., De Bruin, H.A.R., 1983. Temperature measurement with a sonic anemometer and its application to heat and moisture fluxes. Boundary-Layer Meteorology 26, 81–93.

Schrier-Uijl, A.P., Kroon, P.S., Hensen, A., Leffelaar, P.A., Berendse, F., Veenendaal, E.M. Comparison of chamber and eddy covariance based CO_2 and CH_4 emission estimates in a heterogeneous grass ecosystem on peat. Agricultural and Forest Meteorology, submitted for publication.

Schuitmaker, A., 2008. Measurements of turbulent energy spectra in the stable atmospheric boundary layer using Laser Doppler Anemometry. MSc thesis. Delft University of Technology, The Netherlands.

Snyder, W.H., Castro, I.P., 1998. The yaw response of hot-wire probes at ultra-low wind speeds. Measurement Science and Technology 9, 1531–1536.

Tummers, M.J., Passchier, D.M., 2001. Spectral analysis of biased LDA data. Measurement Science and Technology 12, 1641–1650.

Tummers, M.J., Passchier, D.M., Bakker, P.G., 2007. Experiments on the turbulent wake of a flat plate in a strong adverse pressure gradient. International Journal Heat and Fluid Flow 28 (1), 145–160.

Van der Wiel, B.J.H., Moene, A.F., De Ronde, W.H., Jonker, H.J.J., 2008. Local Similarity in the stable boundary layer and mixing-length approaches: consistency of concepts. Boundary-Layer Meteorology 128, 103–116.

Van Dijk, A., 2001. Extension to 3D of "The effect of line averaging on scalar flux measurements with a sonic anemometer near the surface" by Kristensen and Fitzjarrald. Journal of atmospheric and oceanic technology 19, 80–82.

Veenendaal, E.M., Kolle, O., Leffelaar, P., Schrier-Uijl, A.P., Van Huissteden, J., Van Walsem, J., Möller, F., Berendse, F., 2007. Land use dependent CO_2 exchange and carbon balance in two grassland sites on eutropic drained peat soils. Biogeosciences 4, 1027–1040.

Wilczak, J.M., Oncley, S.P., Stage, S.A., 2001. Sonic anemometer tilt correction algorithms. Boundary-Layer Meteorology 99, 127–150.

Wilson, K., Goldstein, A., Falge, E., Aubinet, M., Baldocchi, D., Berbigier, P., Bernhofer, C., Ceulemands, R., Dolman, H., Field, C., Grelle, A., Ibrom, A., Law, B.E., Kowalski, A., Meyers, T., Moncrieff, J., Monson, R., Oechel, W., Tenhunen, J., Valentini, R., Verma, S., 2002. Energy balance closure at FLUXNET sites. Agricultural and Forest Meteorology 113, 223–243.

Wyngaard, J.C., Zhang, S., 1985. Transducer-shadow effects on turbulence spectra measured by sonic anemometry. Journal of Atmospheric and Oceanic Technology 2, 548–558.